Check for updates

Pyrazolone-type compounds: synthesis and *in silico* assessment of antiviral potential against key viral proteins of SARS-CoV-2†

Jovica Branković,[a] Vesna M. Milovanović, [ID][b] Dušica Simijonović, [ID][c] Slađana Novaković,[d] Zorica D. Petrović, [ID][a] Snežana S. Trifunović,[e] Goran A. Bogdanović [ID][d] and Vladimir P. Petrović [ID] *[a]

Coronavirus outbreak is still a major public health concern. The high mutation ability of SARS-CoV-2 periodically delivers more transmissible and dangerous variants. Hence, the necessity for an efficient and inexpensive antiviral agent is urgent. In this work, pyrazolone-type compounds were synthesised, characterised using spectroscopic methods and theoretical tools, and evaluated *in silico* against proteins of SARS-CoV-2 responsible for host cell entry and reproduction processes, *i.e.*, spike protein (S), M^{pro}, and PL$_{pro}$. Five of twenty compounds are newly synthesised. In addition, the crystal structure of a pyrazolone derivative bearing a vanillin moiety is determined. The obtained *in silico* results indicate a more favourable binding affinity of pyrazolone analogues towards M^{pro}, and PL$_{pro}$ in comparison to drugs lopinavir, remdesivir, chloroquine, and favipiravir, while in the case of S protein only lopinavir exerted higher binding affinity. Also, the investigations were performed on ACE2 and the spike RBD-ACE2 complex. The obtained results for these proteins suggest that selected compounds could express antiviral properties by blocking the binding to the host cell and viral spreading, also. Moreover, several derivatives expressed multitarget antiviral action, blocking both binding and reproduction processes. Additionally, *in silico* ADME/T calculations predicted favourable features of the synthesised compounds, *i.e.*, drug-likeness, oral bioavailability, as well as good pharmacokinetic parameters related to absorption, metabolism, and toxicity. The obtained results imply the great potential of synthesised pyrazolones as multitarget agents against SARS-CoV-2 and represent a valuable background for further *in vitro* investigations.

[a]*University of Kragujevac, Faculty of Science, Department of Chemistry, R. Domanovića 12, 34000 Kragujevac, Serbia. E-mail: vladimir.petrovic@pmf.kg.ac.rs*

[b]*University of Kragujevac, Faculty of Agronomy, Department of Chemistry and Chemical Engineering, Cara Dušana 34, 32000 Čačak, Serbia*

[c]*University of Kragujevac, Institute for Information Technologies Kragujevac, Department of Science, Jovana Cvijića bb, 34000 Kragujevac, Serbia*

[d]*University of Belgrade, "VINCA" Institute of Nuclear Sciences-National Institute of the Republic of Serbia, Department of Theoretical Physics and Condensed Matter Physics, 11001 Belgrade, Serbia*

[e]*University of Belgrade, Faculty of Chemistry, Studentski trg 12–16, 11000 Belgrade, Serbia*

† Electronic supplementary information (ESI) available. CCDC 2132092. For ESI and crystallographic data in CIF or other electronic format see https://doi.org/10.1039/d2ra02542f

Introduction

The viral strain SARS-CoV-2 causing severe acute respiratory disease remains a major public health concern. According to the statistical data acquired from World Health Organization (WHO), up to this point, a total of 520 million cases of COVID-19 have been confirmed, including approximately 6.3 million deaths reported worldwide. New viral forms are periodically emerging, which are feared to be more contagious, transmissible, and dangerous than previous strains. The WHO and U.S. Centers for Disease Control and Prevention (CDC) declared the Delta (B.1.617.2) and Omicron (B.1.1.529) strains as "variants of concern". The risk for hospitalisation was doubled for the patients infected with delta variant, in comparison with those infected with alpha.[1] Furthermore, the omicron variant possesses the ability to evade immunity from prior infection.[2,3] Recent findings indicate that omicron can dodge the neutralizing antibodies in vaccinated individuals.[4–7] Enormous efforts were made in vaccine development to repress the coronavirus outbreak. Even with more than 11.6 billion vaccine doses administered globally, the COVID-19 situation is still complicated. As an aggravating circumstance, the SARS-CoV-2 high mutation ability could influence vaccine effectiveness.[8] Regarding this, the potent antiviral compound may overcome this challenge and contribute to the fight against coronavirus.[8] Different strategies were employed to face the COVID-19 emergency, including the prevention of synthesis of viral RNA.[9] The SARS-CoV-2 comprises two overlapping polyproteins (pp1a and

pp1ab) encoded with ∼30 kb RNA genome, which cleavage is essential for replication and transcription processes.[10–13] These cleavage processes are regulated by non-structural viral proteins, such as the main protease M[pro] (also known as 3-chymotrypsin-like protease 3CL[pro]) and papain-like protease PL[pro].[8–11] The M[pro] protein is a homodimer structure, where the substrate-binding site consists of five sub-pockets responsible for the proteolytic activity through a multi-step mechanism, involving an uncommon Cys145–His41 catalytical dyad with the help of a water molecule.[8,9] Compound interacting with catalytic amino acid residues of these subpockets can inhibit the proteolytic action of SARS-CoV-2 main protease.[12] Furthermore, the M[pro] divides the polypeptide chain after Gln residue, unlike all known human proteases.[14] Hence, these atypical features and the engagement in the viral lifecycle designated M[pro] as an attractive antiviral target.[10–12,15] Similarly, the cysteine protease (PL[pro]) is engaged in multiple processes linked with viral maturation and spread, as well as in mechanisms of evasion host antiviral immune response.[16,17] On the other hand, inhibition of the receptor-binding processes and blocking the entry into the host cell are also part of antiviral strategies. SARS-CoV-2 invades human cells *via* interaction of the homotrimeric transmembrane spike-shaped (S) glycoprotein located on the virion surface with extracellular domains of the host angiotensin-converting enzyme 2 (ACE2) receptor.[18] ACE2 is linked with a variety of physiological functions and is extensively expressed in the lungs, cardiovascular system, gut, kidneys, central nervous system, and adipose tissue.[19] Two functional subunits of spike protein, S1 and S2, empower the entry of the viral cell. The receptor-binding domain (RBD) is located in the S1 subunit, whereas the S2 is involved in the membrane fusion processes.[20] Furthermore, SARS-CoV-2 possesses the ability to facilitate its cell entry by exploiting host cell proteases, such as cathepsin, elastase, furin, and transmembrane protease serine 2.[19] Such unusual behaviour of the SARS-CoV-2 virus triggered the various approaches in the search for potential antiviral candidates, *i.e.* computational screening of existing drugs, drug repurposing, and *in silico* design of new potential inhibitors of viral key proteins.[21–24] Molecular docking is also identified as a cost-effective and less time-consuming method for the search of promising antiviral candidates, particularly against SARS-CoV-2.[8,9,12,23,25–27] Such molecular docking analysis identified various potential compounds that can interact with M[pro] and S proteins of virus SARS-CoV-2, including pyrazolone-type compounds.[28,29] Moreover, pyrazolone-based compounds were investigated on the SARS-CoV and MERS-CoV proteases and designated as a good base for the development of antiviral agents.[30,31] Pyrazolone structural motif is frequently utilised for the development of novel hybrid molecules with various biological activities,[32] including antiviral,[33] antioxidant,[34] antimicrobial,[35] analgesic,[36] anti-inflammatory,[37] cytotoxic,[38] and many other activities. Furthermore, these compounds express inhibitory activity on many enzymes, such as cyclooxygenase,[39] phosphodiesterase,[40] carboxylesterase,[41] and α-glucosidase,[42] which also illustrate the versatility of pyrazolone pharmacophore. Their diverse biological activities encouraged us to synthesise a series of pyrazolone

analogues with potential anti-SARS-CoV-2 activity. Molecular docking analyses were performed with viral S, M[pro], and PL[pro] proteins to get insight into the binding affinity with pyrazolone derivatives. On the other hand, the binding of some compound to the RBD-ACE2 complex could block the virus spread.[43] Additionally, some pyrazolones were identified as potent inhibitors of angiotensin-converting enzyme (ACE), which has a number of pathological roles.[44] This prompted us to investigate the binding of selected pyrazolones to human ACE2 cell receptors, as well as to the spike RBD-ACE2 complex, with the idea that in such case, the SARS-CoV-2 cell entry and spreading could also be prevented.
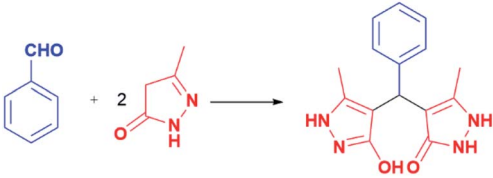
Results and discussion

Synthesis of pyrazolone derivatives

Generally, the literature on these particular types of compounds is relatively scarce, and the research is mainly focused on the development of novel eco-friendly synthetic methods employing various catalysts, mostly ionic liquids and nanoparticles.[45–52] Following such a trend, the synthesis of pyrazolone analogues **a–t** was accomplished in the reactions of 5-methyl-2,4-dihydro-3*H*-pyrazol-3-one with different aromatic aldehydes in the presence of diethanolamine as a catalyst, and in ethanol and under reflux. To optimise reaction conditions, the model reaction between benzaldehyde and 5-methyl-2,4-dihydro-3*H*-pyrazol-3-one was investigated in the presence of various catalysts and solvents (Table 1).
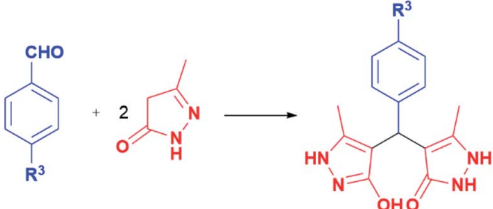
In this model reaction, diethanolamine (DEA), triethanolamine (TEA), and their corresponding acetate salts ([HDEA][OAc] and [HTEA][OAc]) were tested as catalysts, while as solvents water, ethanol, and a mixture of water and ethanol were used. The selection of the corresponding ethanolamine catalysts was based on their known environmental behaviour, *i.e.*, ready biodegradation and low bioaccumulation potential, cost-effectiveness, as well as on their extensive application in industry and common consumer products.[53–55] The reaction progress was monitored using thin-layer chromatography. The optimal time for conversion of starting material in all cases was 3 h. It is worth pointing out, that formation of the product was observed in all tested reactions. However, the results presented in Table 1 pointed out DEA as the most efficient among all tested catalysts, where the best yields were achieved in ethanol as solvent. Furthermore, the presence of groups with electron-donating and the electron-withdrawal effect was considered in the catalyst selection. For that purpose, aromatic aldehydes bearing the –OH and –Cl groups were used, Table 1. The obtained results revealed that the best yields were achieved in the presence of DEA, as well. Based on the obtained results, the optimal conditions for performing the reactions were 20 mol% of DEA as a catalyst, ethanol as solvent, and reflux for 3 h. These reaction conditions were used for the synthesis of pyrazolone derivatives **a–t**. It is important to emphasise that five of twenty analogues (**m, o, q, r**, and **t**) are newly synthesised compounds. To our knowledge, these new compounds were not obtained by previously reported methods, while the other compounds are known.[50,56–60] The products were obtained from good to

Table 1 The optimisation of reaction conditions[a]

Model reaction 1

Reaction conditions and product yields

	H$_2$O	EtOH	H$_2$O : EtOH (1 : 1)
No catalyst	43%	67%	68%
[HDEA][OAc]	54%	77%	68%
DEA	73%	82%	65%
[HTEA][OAc]	70%	73%	70%
TEA	77%	77%	77%

Model reaction 2

Reaction conditions and product yields

R^3		[HDEA][OAc]	DEA	TEA
OH	EtOH	69%	72%	53%
Cl		58%	76%	76%

[a] Reaction conditions: aromatic aldehyde (1 mmol), pyrazolone (2 mmol), catalyst 20 mol%, solvent 3.0 mL, reflux 3 h.

Table 2 Synthesis of pyrazolone derivatives

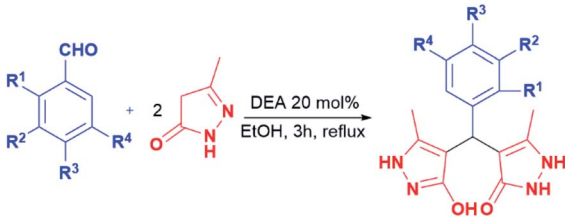| Entry	R^1	R^2	R^3	R^4	Yield (%)
a	H	H	H	H	82
b	OH	H	H	H	64
c	H	OH	H	H	72
d	H	H	OH	H	72
e	H	Cl	H	H	72
f	H	H	Cl	H	76
g	H	H	F	H	70
h	NO$_2$	H	H	H	72
i	H	NO$_2$	H	H	78
j	H	H	NO$_2$	H	85
k	CH$_3$	H	H	H	91
l	H	CH$_3$	H	H	70
m	OH	OH	H	H	45
n	H	OH	OH	H	71
o	OH	OCH$_3$	H	H	61
p	H	OCH$_3$	OH	H	85
q	H	OCH$_3$	OH	OCH$_3$	31
r	H	OH	OCH$_3$	OCH$_3$	31
s	H	OCH$_3$	OCH$_3$	OCH$_3$	87
t	OH	Cl	H	Cl	94

excellent yield, except derivatives **m**, **q**, and **r** which were isolated in 31–45% yields (Table 2).

Characterisation of compounds a–t

All synthesised pyrazolone derivatives were characterised using ^{1}H NMR, ^{13}C NMR, UV-Vis, and FT-IR spectra. Additionally, simulations of IR and UV-Vis spectra were performed to confirm the assignation of experimental bands. All spectra are provided in the ESI.†

In the ^{1}H NMR spectra, for all compounds, the signals originating from methyl groups protons were observed around 2.0 ppm as sharp singlets (Fig. S1–S20†). For the compounds containing methoxy group(s), the peaks that correspond to these protons were noted at around 3.6 ppm. Furthermore, sharp singlets in the 5.1–4.6 ppm region correspond to the proton from the methine group that joints aldehyde and pyrazolone moieties. The signals in the 8.1–6.3 ppm area were assigned to the aromatic protons from the aldehyde moiety.

Depending on the structure of the compound, these protons resonated mostly as sharp singlets, doublets, doublets of doublets, or multiplets. On the other hand, the peaks originating from the phenolic –OH proton were mainly noticed in the 9.0–8.0 ppm region, resonating as sharp or broad singlets. Finally, in the 11.4–11.0 ppm region, broad singlets originating from –OH and –NH groups of the pyrazolone rings were observed. The ^{13}C NMR spectra consist of multiple peaks originating from methyl, methoxy, methinic, and aromatic carbons, as well as those from the pyrazolone unit. Generally, the signals at the highest chemical shifts (above 160.0 ppm) correspond to the carbonyl carbon. In the 160.0–103.0 ppm region multiple signals were found, where those at higher chemical shifts correspond to more substituted carbon atoms, from both aldehyde and pyrazolone moieties (*i.e.*, those bearing –OH, –OCH$_3$, *etc.*). On the other hand, peaks at the lower ppm values in the aforementioned region were assigned to less substituted carbons. For compounds bearing –OCH$_3$ groups, the signals related to methoxy carbon were in the 60.0–55.0 ppm area. Finally, around 10.0 ppm, the signals from the carbon of the methyl group were observed, whereas those from the methine group were noted near 32.0 ppm.

Generally, all IR spectra share a great resemblance, which is indicating the similar structure of all compounds. Moreover, a high agreement between experimental and simulated spectra was achieved (Fig. S24–S28†). Here, the bands located in the

3600–3200 cm^{-1} region were assigned to the O–H and N–H stretching vibrations. Furthermore, aromatic C–H stretching vibrations were identified somewhat above 3000 cm^{-1}, while the bands originating from aliphatic C–H were observed in the region from 3000 cm^{-1} to 2800 cm^{-1}. The bands located around 1600 cm^{-1} originate from C=O stretching vibration, whereas those near 1530 cm^{-1} are assigned to the stretching vibration of the C=N bond. Also, the bands around 1500 cm^{-1} and 1450 cm^{-1} were identified because of bending HCC and C=C stretching vibrations, while those in the 1400–1350 cm^{-1} region were assigned to the bending HNN and HOC. In the 1330–1000 cm^{-1} multiple bands were identified, such as stretching C–O, C=C, and N–N, whereas below 1000 cm^{-1} the bands originating from torsion HOCC, HNCC, and HCCC vibrations were mainly observed. Also, for analogues bearing –NO$_2$, –F, and –Cl groups, the bands originating from stretching N=O, C–F, and C–Cl were identified.

The experimental UV-Vis spectra were in excellent agreement with simulated ones (Fig. S29–S33†). For the newly synthesised compounds, Kohn–Sham orbitals were constructed to identify the electronic transitions responsible for the appearance of experimental bands (Fig. S34–S38†). Generally, the experimental UV-Vis spectra revealed absorption bands around 202, 230, 250, and 280 nm. The electronic transitions for the newly synthesised compound **o** are presented in Table 3, while transitions for the other new compounds (**m**, **q**, **r**, and **t**) are provided in Table S1.† The electronic transitions were arranged in descending order of contribution. For compound **o**, the absorption band at 282 nm is a consequence of HOMO to LUMO electronic transition. In all cases, the bands around 250 nm mainly originate from HOMO to LUMO and HOMO−1 to LUMO transitions. For compounds **m**, **o**, and **r**, the bands around 230 nm mostly originate from HOMO−3 to LUMO transition. In the case of **t**, the band at 232 nm was assigned to HOMO−1 to LUMO−1, whereas for **q** the band at 230 nm mainly corresponds to HOMO−4 to LUMO transition. For compounds **m**, **o**, and **q**, the bands around 202 nm primarily originate from transitions to high-level LUMOs, such as LUMO+4, LUMO+5, LUMO+6, and LUMO+7. On the other hand, for compounds **r**

and **t**, these bands appeared as a consequence of the electronic transitions from low-level HOMOs (HOMO−4, HOMO−5, and HOMO−6) to LUMO, LUMO+1, and LUMO+2.

Crystal structure analysis

The crystal structure of compound **p** is given in Fig. 1, while selected bond lengths and valence angles are listed in Table 4, which are here reported for the first time. To our knowledge, crystal data on these particular compounds are insufficient. Moreover, all articles related to these compounds presented the OH-tautomeric forms of both pyrazolone rings,[45–52] including the crystal structure of compound **a**.[57] Single crystal X-ray analysis shows that the compound consists of a substituted phenyl ring and two 3-methyl-5-pyrazolone rings connected through the benzyl C1 atom. The two pyrazolone fragments are present in keto–enol tautomeric forms. The carbonyl acceptor and hydroxy donor resulting from tautomerisation suitably orient to form a strong intramolecular O2–H···O1 hydrogen bond which stabilises this crystal structure (Fig. 1). The phenyl ring is nearly symmetrically positioned with respect to the pyrazolone rings. Thus, the dihedral angle between the phenyl and N–H, and the phenyl and O–H pyrazolone ring is 77.26(7) and 70.85(7)°, respectively. The dihedral angle between the
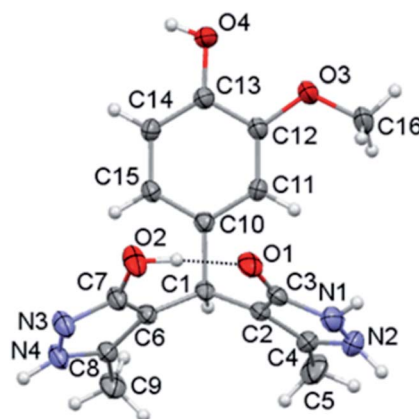

Fig. 1 Crystal structure of molecule **p**. Thermal ellipsoids are shown at the 30% probability level.

Table 3 Electronic transitions for compound **o**

λ (nm)	Transition	
282	HOMO	LUMO
249	HOMO	LUMO
	HOMO−1	LUMO
	HOMO	LUMO+1
227	HOMO−3	LUMO
	HOMO−1	LUMO+1
	HOMO−2	LUMO
	HOMO−1	LUMO+3
	HOMO	LUMO+3
	HOMO−2	LUMO+1
202	HOMO−2	LUMO+5
	HOMO−2	LUMO+6
	HOMO−4	LUMO+1
	HOMO−6	LUMO
	HOMO−1	LUMO+6

Table 4 Selected bond distances and angles (Å, °)

Bond		Angle	
C3–O1	1.267(3)	N1–N2–C4	107.6(2)
C7–O2	1.346(3)	N3–N4–C8	112.5(2)
N1–C3	1.355(3)	C3–N1–N2	109.4(2)
N2–C4	1.358(3)	C7–N3–N4	112.5(2)
N3–C7	1.327(3)	C2–C3–N1	106.3(2)
N4–C8	1.340(3)	C6–C7–N3	111.9(2)
N1–N2	1.371(4)	C1–C2–C3	125.9(2)
N3–N4	1.354(3)	C1–C6–C7	129.4(2)
C2–C3	1.424(3)	C2–C1–C6	114.6(2)
C2–C4	1.364(3)	C10–C1–C6	112.6(2)
C6–C7	1.412(3)	C10–C1–C2	111.5(2)
C6–C8	1.375(3)	C11–C10–C1	120.8(2)

Table 5 Geometry of hydrogen bonds[a]

D–H⋯A	D–H (Å)	H⋯A (Å)	D⋯A (Å)	D–H⋯A (°)	Symmetry codes
O2–H1⋯O1	0.94(5)	1.64(5)	2.579(3)	174(4)	x, y, z
N4–H1n4⋯O1	0.93(3)	1.93(4)	2.842(3)	168(3)	$x - 1/2, y, -z + 1/2$
N1–H1n1⋯O3	0.85(4)	2.58(3)	3.164(3)	127(3)	$-x + 1/2, y - 1/2, z - 1/2$
N1–H1n1⋯O4	0.85(4)	1.95(4)	2.777(3)	164(3)	$-x + 1/2, y - 1/2, z - 1/2$
O4–H1o4⋯N3	0.82(4)	1.83(4)	2.648(3)	169(4)	$-x, y + 1/2, -z + 1$
C9–H9a⋯Cg1	0.96	3.05	3.769(3)	132	$x + 1/2, y, -z + 1/2$
C16–H16a⋯Cg2	0.96	3.20	3.919(3)	133	$-x, y + 1/2, -z$

[a] Cg1 = C10/C15; Cg2 = N3/C7.

pyrazole rings is 47.44(10)°. The bond distances and angles in **p** are in good agreement with the values of previously reported crystal structures, comprising similar set of rings.[61–64] The different position of proton in two pyrazolones is primarily re-flected in the lengths of C3–O1 and C7–O2 bonds (Table 4), also the bonds vicinal to protonated N1 atom are slightly longer in comparison to those involving deprotonated N3 atom. Valence angles at benzyl C1 atom notably deviate from the regular tetrahedral geometry (Table 4). The strong intramolecular O2–H⋯O1 hydrogen bond formed between hydroxy and carbonyl residues is a specific feature of this crystal structure (Fig. 1).

The eight-membered S(8) ring motif[65] formed in this way partly locks the orientation of the pyrazolone rings with an almost linear distribution of the donor and acceptor sites. In the crystal packing the molecules arrange by strong intermo-lecular O–H⋯N and N–H⋯O hydrogen bonds (Table 5).

The packing can be described in terms of $R_3^3(9)$ hydrogen bonded trimers which mutually connect to form a complex three-dimensional network (Fig. 2). The three strong hydrogen

bonds joined in the trimer, individually define chains extending in a particular direction. Thus, the strongest interaction in the system O4–H⋯N3 arranges the molecules into a zig-zag chain extending along the *b* crystallographic axis, while the N4–H⋯O1 interaction formed between the pyrazolone rings builds the chain along *a* crystallographic axis. Finally, the pyrazolone donor N1–H1 interacts with the O⋯O donor system formed by phenyl ring substituents[66] and connects the molecules in [011] direction (Fig. 2).

In silico inhibitory activity towards SARS-CoV-2 proteins

All pyrazolones **a–t** were subjected to *in silico* investigation of potential antiviral activity against SARS-CoV-2. Molecular docking was performed on the protein responsible for attach-ment of the virus to the host cells (glycoprotein spike protein (S)), as well as on proteins involved in viral reproduction processes (main protease (M^{pro}), and papain-like protease (PL$_{pro}$)). Also, docking was conducted on human cell receptor angiotensin-converting enzyme-related carboxypeptidase
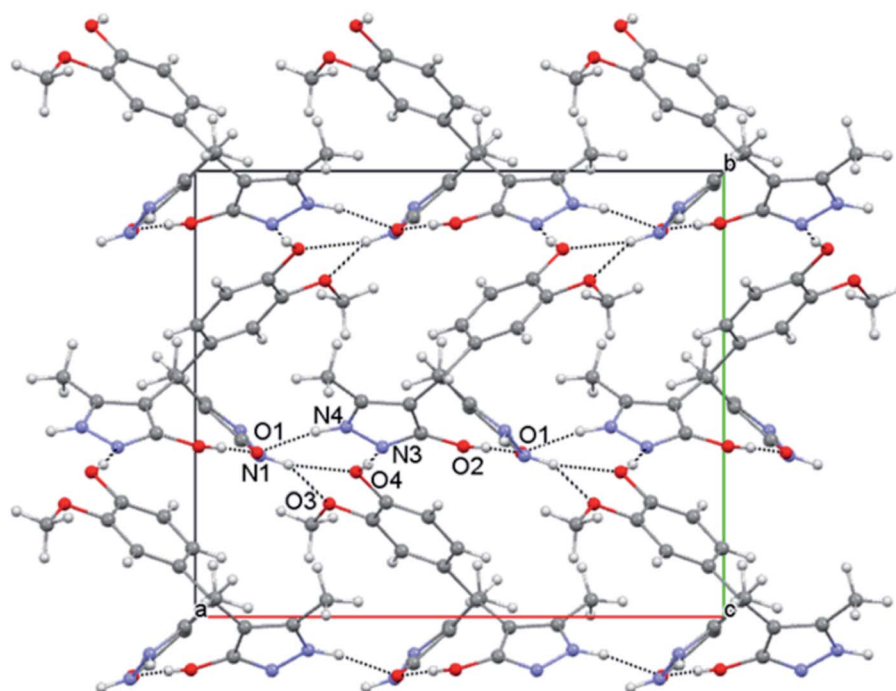

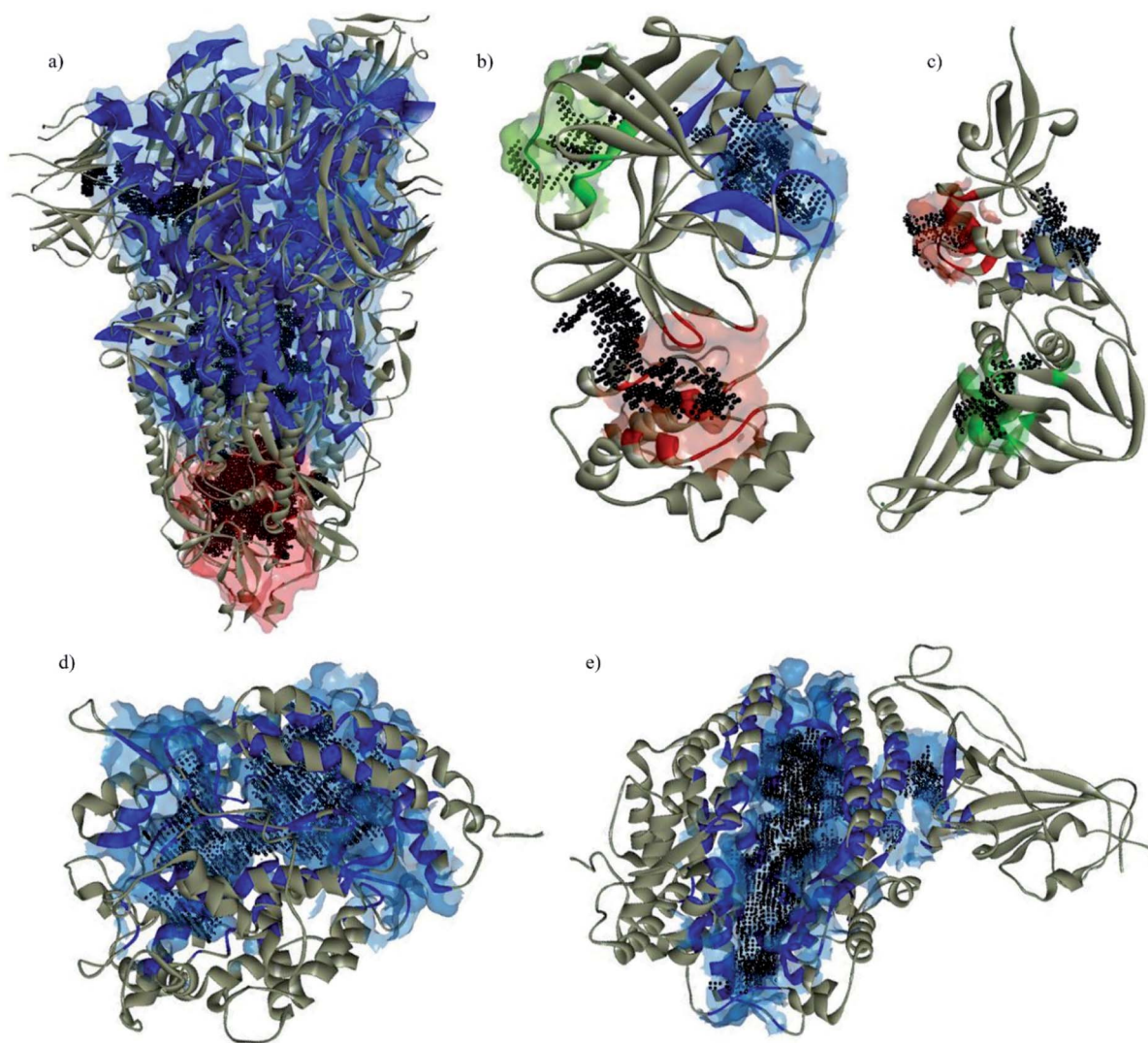**Fig. 2** View of the molecular packing with the strongest hydrogen bonds.

Fig. 3 Active site pockets predicted by CastP server (blue, red, and green surfaces) and CHARMM-GUI (black dots) of the investigated proteins: (a) spike; (b) M^{pro}; (c) PL$_{pro}$; (d) ACE2; (e) spike RBD-ACE2 complex.

(ACE2), and on spike receptor-binding domain complexed with its receptor ACE2 (Spike RBD-ACE2). Blind docking was performed for all proteins and all compounds. Such an approach was chosen over site-specific docking to get the full insight. Furthermore, CastP server[67] and CHARMM-GUI[68] were used for the prediction of active site pockets and respective amino acid residues (Fig. 3). Good agreement between these two predictions was achieved. It is important to emphasise that all compounds were positioned within the predicted pockets of investigated proteins.

SARS-CoV-2 spike glycoprotein (S). The docking results obtained for compounds **a–t** and S protein revealed that the derivatives **j** and **i** exerted the highest binding affinity of −9.3 and 9.0 kcal mol^{-1} (Fig. 4a and Table S3†). Both compounds were placed between the trimerisation helices of protomeric chains A and C. Four hydrogen bonds were established between compounds **j** and **i** and spike protein helices C. With chain A, one hydrogen bond is established between the –NH group of

pyrazolone ring B and carbonyl peptide group of Gln1036 (dHB = 2.49), while the other one is formed by carbonyl group of pyrazolone ring A and –NH group of Trp886 (dHB = 2.12 Å). The same pyrazolone ring A carbonyl group is hydrogen-bonded to the –OH of the side chain of Tyr1047 from protomer C (dHB = 3.03 Å), that way forming a three-center hydrogen bond. The nitro group of pyrazolone ring C establishes strong hydrogen bonding with the peptide bond –NH of His1048 of the chain C (dHB = 2.05 Å). In addition to these, the π-donor hydrogen bond between the indole side chain of Trp886 of the protomer A and –OH group of the pyrazolone ring B was established, also (π-donor – H–O). The same amino acid side chain is involved in electrostatic π–π T-shaped interaction with the π-electrons from the ring B of compound **j**, as well as between Tyr1047 of the protomer C and aromatic ring C. The π–π T-shaped interaction was also established between Tyr904 (A) with ring A. Hydrophobic alkyl interaction of the Lys1038 (protomer C) and methyl group of the ring B round-up established contacts
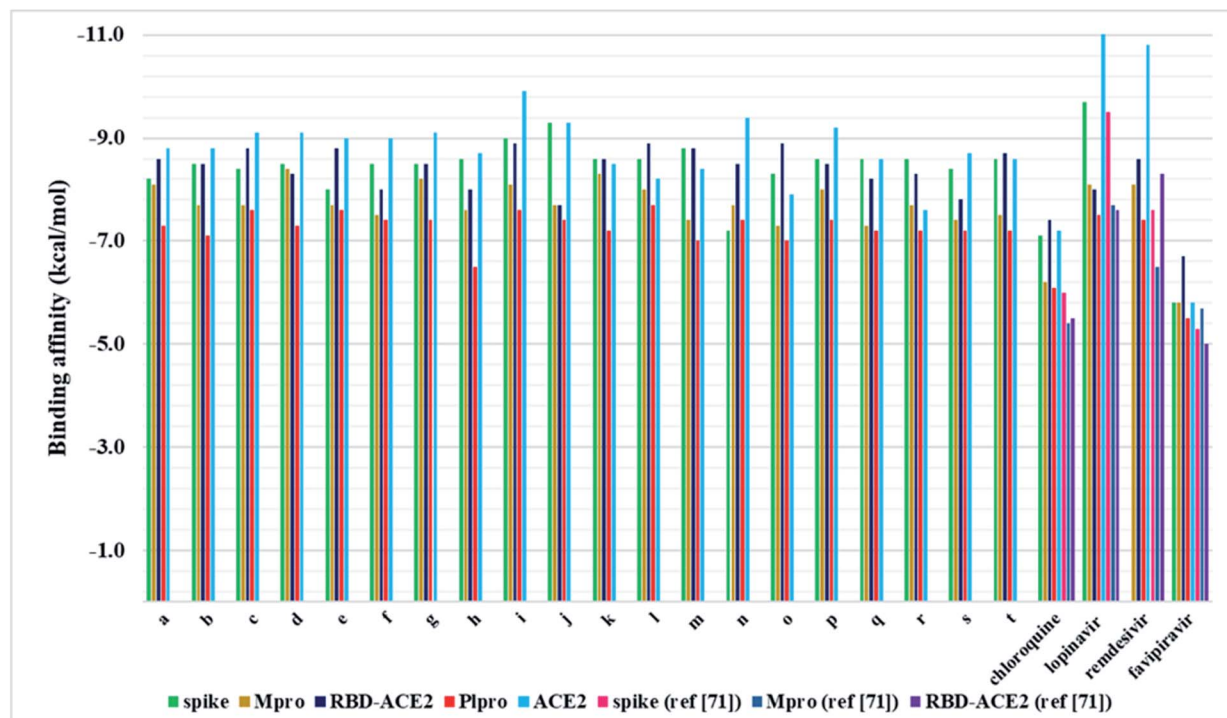
Fig. 4   Binding modes of FDA-approved drugs and pyrazolones (left), insight into the binding of the best-screened pyrazolones (middle), and 2D interaction plot of the best-screened compounds (right) to the: (a) spike, (b) M^{pro}, and (c) PL$_{pro}$.

Fig. 5 Graphical interpretation of binding affinities for compounds **a–t** and FDA-approved drugs towards selected proteins.

between S protein and compound **j**. It is worth pointing out that R^2, R^3, R^4-trisubstituted pyrazolones **q**, **r**, and **s** didn't dock at the same position as all other compounds. This is most likely due to the voluminosity of the substituents of the ring C. Namely, compounds **q** and **r** bear two methoxy groups and one hydroxy group, while **s** possess three methoxy groups. The obtained docking energies were compared to the binding affinities of the selected approved drugs: lopinavir, chloroquine, remdesivir, and favipiravir (Fig. 5).[69] It is important to emphasise that, from the group of the FDA-approved drugs, only lopinavir exerted lower binding energy than compound **j** (-9.5 kcal mol^{-1}, Table S3†), and that except **n**, all pyrazolones expressed a higher tendency to bind to the S protein than chloroquine, remdesivir, and favipiravir. In addition, selected drugs were subjected to the docking study. Compared to the available literature data, somewhat higher binding affinities were obtained for these drugs (Fig. 5 and Table S3†). However, the same trend in binding affinities was obtained.

SARS-CoV-2 main protease (M^{pro}). The catalytically active pocket of M^{pro} has been mainly preserved among all coronaviruses.[70] It has been shown that helical domain III suffered the most significant changes, while the catalytically active pocket (between domains I and II) is practically unchanged.[10] Bearing this in mind, it is reasonable to expect that compounds preferably binding to pocket 1 could possess the ability to interact with multiple coronavirus strains. Here, all investigated pyrazolones occupied pocket 1 of the M^{pro} protein (Fig. 3b and 4b). Compounds **d** and **k** exerted the highest binding affinity of -8.4 and -8.3 kcal mol^{-1}. The interaction analysis of the best-screened analogue **d** with the M^{pro} revealed four hydrogen

bonds. Here, the –NH (ring A) of compound **d** established a hydrogen bond with the carbonyl group of Glu166 (dHB = 2.62 Å). On the other hand, ring B is involved in three hydrogen bonds. –NH of this ring was hydrogen-bonded to the oxygen of the Glu166 side chain (dHB = 2.61 Å) and to the peptide oxygen of Phe140 (dHB = 2.07 Å). This way bifurcated three-centered O⋯H(N)⋯O hydrogen bond is formed. The remaining hydrogen bond was established between –NH of the His163 side chain and the other nitrogen atom of the ring B (dHB = 2.05 Å). Moreover, the π-donor hydrogen bond between –NH of Glu166 and π-electrons of the pyrazolone ring A was established, as well as the C–H⋯O carbon hydrogen bond between α C–H of Met165 and the carbonyl oxygen of the ring A. Among approved drugs, lopinavir exerted the highest affinity towards M^{pro} with the binding energy of -7.7 kcal mol^{-1}.[69] The binding affinities of all other pyrazolones were higher or close to the binding affinity of lopinavir (Fig. 5 and Table S3†), implying their potential usage as M^{pro} blockers. In addition, lopinavir, chloroquine, remdesivir, and favipiravir were redocked to reclaim the binding energies (Fig. 5 and Table S3†). Similar to the case of redocking with the S protein, somewhat lower binding energies were obtained. However, the binding affinity of derivative **d** was higher than any of the obtained affinities for the screened FDA-approved drugs.

SARS-CoV-2 papain-like protease (PL$_{pro}$). All compounds preferred one position of the PL$_{pro}$, *i.e.*, the active site pocket 3 (Fig. 3c and 4c). Among the pyrazolones, compound **l** exhibited the highest binding affinity of -7.7 kcal mol^{-1} (Table S3†). It is worth mentioning that pyrazolones **c**, **e**, and **i** displayed at least comparable binding energies of -7.6 kcal mol^{-1}. Nevertheless,

analogue **l** was engaged by two hydrogen bonds established between the oxygen of the Thr301 side chain and –NH of the ring A (dHB = 2.58 Å), as well as between the peptide carbonyl group of Asn267 and –OH group of ring B (dHB = 2.25 Å). Asn267 is also contributing with amide–π stacked interaction, established with the ring C of compound **l**. Asp164 is contributing to the binding of **l** with side-chain carboxylic group interaction with π bonds of pyrazolone rings A and B (π–charge interactions). The side chains of Pro247 and Pro248 were involved in hydrophobic alkyl interactions with the methyl group of ring A. In addition, the side chain of Pro248 is involved in alkyl–π interactions with the π electrons from rings A and C. Similarly, Leu162 is interacting with π electrons from ring B. Comparison with the binding affinities of the selected FDA-approved drugs revealed that pyrazolone **l** exerts higher binding affinity than any of these drugs (Fig. 5 and Table S3†). Moreover, pyrazolones **c**, **e**, and **i** binding energies are lower than that of the best-screened drug lopinavir (−7.5 kcal mol⁻¹), and the second one remdesivir (−7.4 kcal mol⁻¹). It is worth pointing out that all pyrazolones exerted higher binding affinities towards PL_{pro} than chloroquine and favipiravir.

Human angiotensin-converting enzyme-related carboxypeptidase (ACE2). Besides the inhibition of the SARS-CoV-2 proteins, one of the ways to prevent the spreading of the virus in the human host cell is inhibition of its angiotensin-converting enzyme-related carboxypeptidase (ACE2) (Fig. 3d). Namely, this enzyme serves as a receptor for the S protein of the virus.[71] *In silico* study revealed that derivative **i** exerts the highest binding affinity towards ACE2 of −9.9 kcal mol⁻¹, Table S3.† Here, multiple interactions of **i** with ACE2 were observed (Fig. 6a). Firstly, the formation of seven hydrogen bonds was noted. Each of the oxygens from the nitro group on ring C formed two bifurcated hydrogen bonds. One oxygen atom of the nitro group (ring C) formed hydrogen bonds with the –NH of the imidazole side chains of His345 (dHB = 2.56 Å) and His505 (dHB = 2.74 Å), completing the three-center hydrogen bond (N–H⋯O⋯H–N). The same imidazole –NH of His505 established a hydrogen bond with the second oxygen of the nitro group (dHB = 2.98 Å), forming that way another three-center hydrogen bond (O⋯N–H⋯O). Also, this oxygen forms a hydrogen bond with the –NH side-chain group of Arg273 (dHB = 1.98 Å). The –OH group of the ring B formed a hydrogen bond with the side-chain oxygen of the Thr371 (dHB = 2.59 Å). Moreover, the same oxygen of the Thr371 established a hydrogen bond with the carbonyl oxygen of ring A (dHB = 2.37 Å). The –NH of the pyrazolone ring B formed a strong hydrogen bond with the oxygen of the Glu406 side chain's carboxylic group (dHB = 2.30 Å). In addition to these, electrostatic π–anion (the ring B–Glu406) and π–cation (the ring C–Arg518) were present. Furthermore, hydrophobic π–π stacked (Phe274–ring B) and π–π T-shaped (His374–ring C), as well as π–σ (Phe274 and methyl group of the ring B) and π–alkyl (ring A π-electrons and side chain of Leu370, as well as Phe274 with ring A methyl group) interactions encapsulate the main skeleton of the pyrazolone **i**. Compared to the FDA-approved drugs (Fig. 5 and Table S3†), lopinavir and remdesivir exerted higher binding affinities (−11.2 and −10.8 kcal mol⁻¹), while the binding affinities of

chloroquine and favipiravir were considerably lower (−7.2 and −5.8 kcal mol⁻¹).

Spike receptor-binding domain complexed with its receptor ACE2 (spike RBD-ACE2). The receptor-binding domain (RBD), which is part of the S1 protomer of the spike, is responsible for recognition and interaction with the ACE2 (Fig. 3e). The obtained docking results for spike RBD-ACE2 complex pointed out compounds **i**, **o**, and **l** as the most potent binders with binding energies of −8.9 kcal mol⁻¹. The obtained results indicated a higher affinity of **i**, **o**, and **l** towards spike RBD-ACE2 than selected drugs (Fig. 5 and Table S3†).[69] Since pyrazolones were positioned in the same chamber, compounds **i**, **o**, and **l** formed three same hydrogen bonds: with the peptide carbonyl group of Ala396 *via* –NH of ring A (dHB = 2.30, 2.36, and 2.36 Å, respectively); with the peptide carbonyl group of Lys562 by second –NH of the ring A (dHB = 2.24, 2.27, and 2.13 Å, respectively); and with peptide –NH group of Trp566 *via* carbonyl group of the ring A (dHB = 2.15, 2.10, and 2.15 Å, respectively) (Fig. 6b). Furthermore, –OH groups of the ring B of **i**, **o**, and **l** were hydrogen-bonded with carbonyl groups of Gly205, Glu208, and Asp206, respectively (dHB = 2.26, 2.27, and 2.22 Å, respectively). Owing to the different substitution of the ring C, an additional hydrogen bond between Asn210 and nitro group was observed for compound **i** (dHB = 2.36 Å), whereas in the case of **o**, the hydrogen bond between Glu208 and phenolic –OH group was noted (dHB = 1.86 Å). For compound **l**, due to the absence of hydrogen bond donor/acceptor on ring C, no additional hydrogen bonds were noted. On the other hand, in all cases, the π – donor hydrogen bond was established between ring C and Asn210. All compounds were involved in π–cation electrostatic interaction between π-electrons from ring B and the side chain of Lys562. Moreover, all compounds established hydrophobic interactions: π–σ between ring C π-electrons and Leu95, π–alkyl between π-electrons of ring A and Lys562, as well as between π-electrons of ring C and Val209 and Pro565, and alkyl interactions between methyl group of ring A and Leu95 and Lys562. Unlike compound **l**, ring B methyl group of compounds **i** and **o** established alkyl interactions with Leu95.

In silico ADME/T profile

Drug-likeness and absorption. All pyrazolone analogues were submitted to *SwissADME* and *pkCSM in silico* investigations to evaluate their pharmacokinetics and drug-like nature. Lipinski's rule of five represents a way to estimate the drug-likeness of the investigated compound. This rule suggests that an orally bioactive drug should possess less than five hydrogen bond donors and ten hydrogen bond acceptors, as well as a molecular mass of less than five hundred Daltons and the logarithm of the octanol–water partition coefficient (Log $P_{o/w}$) less than five.[72] Log $P_{o/w}$ parameter describes the compound's lipophilicity, which is an important feature for drug absorption. In addition to these rules, Ghose and Veber's criteria are extended to molecular refractivity (40–130 range), number of atoms (from 20–70), number of rotatable bonds (ten or fewer), and polar surface area (no greater than 140 Å²).[73,74] The results obtained by *SwissADME* revealed that basically, all pyrazolones meet these
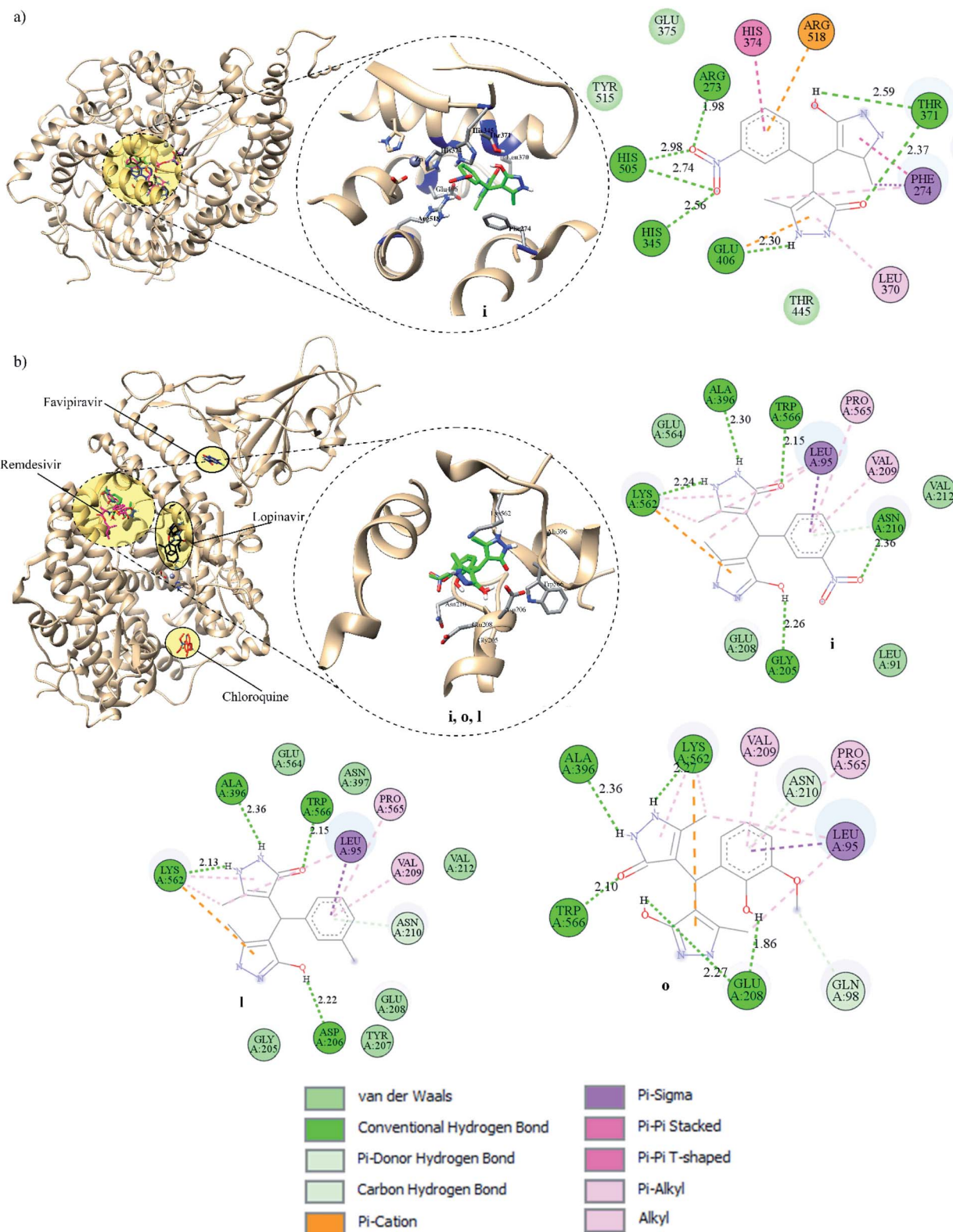
Fig. 6 Binding modes of FDA-approved drugs and pyrazolones, insight into the binding of the best-screened pyrazolones, and 2D interaction plot of the best-screened compounds to the (a) ACE2 and (b) Spike RBD-ACE2 complex.

criteria, with some minor violations (Tables S4–S8†). Additionally, most compounds fulfil the Egan and Muegge requirements. Also, the *SwissADME* oral bioavailability radar, which

illustrates the optimal range of each property, showed that pyrazolones generally fulfil the requirements, with some slight saturation and polarity deviations (Fig. S39–S42†).

The values of Log $P_{o/w}$ were calculated by different methods (iLOGP, XLOGP3, WLOGP, MLOGP, and Silicos-IT Log P). According to the obtained results, all compounds meet the lipophilicity criteria (Tables S4–S8†). Also, water solubility is an important element for absorption. Three methods (ESOL Log S, Ali Log S, and Silicos-IT Log S_w) were used for the calculation of water solubility descriptors. Depending on the calculation method, all pyrazolone analogues were predicted to be soluble or moderately soluble in water (Tables S4–S8†).

The *SwissADME* Brain Or IntestinaL EstimateD permeation method (BOILED-Egg) predicted high gastrointestinal absorption for almost all compounds (Tables S4–S8†). Similarly, *pkCSM* prediction of the human intestine absorption percentage for all pyrazolones was in the range of 61.5–76.5% (Tables S9–S28†). Finally, it is important to point out that *pkCSM* categorised all pyrazolones as P-glycoprotein substrates (Tables S9–S28†). P-glycoprotein (P-gp) is an ATP binding cassette transporter involved in drug uptake and efflux, influencing their plasma and tissue concentrations.[75] Here, the substrates of P-gp can act as inhibitors or inducers, where the inhibition of P-gp increases drug bioavailability, while induction reduces it.[75] The results obtained by *SwissADME* differ, *i.e.*, most pyrazolones were not identified as P-gp substrates (Tables S4–S8†).

Distribution. The volume of distribution (VDss) was predicted for each compound (Tables S9–S28†). This parameter illustrates the drug's tendency to stay in plasma or to redistribute to other tissue segments.[76] Basically, a higher value of VDss indicates that a higher amount of drug is necessary to reach a given plasma concentration.[76] Generally, *pkCSM* predicted log VDss in the range of −0.2 to 0.8 (values below −0.15 are considered low, whereas those above 0.45 are high) (Tables S9–S28†). Furthermore, drugs in plasma exist in the unbound/bound state to serum proteins equilibrium, which may affect drug efficiency, *i.e.*, the more that is bound-the less efficient is drug distributed. Here, the *pkCSM* predicted fraction unbound (fu) values for all compounds were in the range from 0.17 to 0.31 (Tables S9–S28†).

The blood–brain barrier (BBB) represents a structure that protects the brain from exogenous factors.[77] The ability of drugs to permeate BBB is an important parameter for side effects/toxicity considerations.[77] Based on the obtained results, both *SwissADME* and *pkCSM* predicted that pyrazolones are not able to permeate BBB (Tables S4–S8†). Also, the CNS permeability was predicted according to the log PS values (blood–brain permeability-surface area product). Here, compounds with log PS higher than −2.0 penetrate CNS, whereas those below −3.0 are designated as unable. The *pkCSM* obtained results for log PS were in the −3.0 to −2.0 range (Tables S9–S28†).

Metabolism. The metabolism of pyrazolones **a–t** was estimated using *SwissADME* and *pkCSM* (Tables S4–S28†). Here, the interactions with the cytochrome P450 enzyme family (CYP1A2, CYP2C19, CYP2C9, CYP2D6, CYP3A4) were observed since these enzymes play a crucial role in drug metabolic transformations and elimination. Therefore, their inhibition would lead to undesirable adverse effects related to drug low clearance and accumulation.[25,78] Two main isoforms that are responsible for drug metabolism are CYP3A4 and CYP2D6.[77] According to

SwissADME, among all investigated compounds, only derivative **s** was predicted to have inhibitory activity on CYP3A4, whereas for CYP2C9 and CYP2D6 no inhibitory activity was observed. On the other hand, half of the investigated compounds could potentially inhibit CYP2C19, whereas for CYP1A2 most compounds were not likely to act as inhibitors. Similar results were observed in *pkCSM* predictions.

Excretion. The prediction of excretion was achieved using *pkCSM*, according to the logarithm of the total clearance parameter (log ml^{-1} min^{-1} kg^{-1}) and renal organic cation transporter 2 (OCT2) substrate category (Tables S9–S28†). The predicted total clearance values were in the range of −0.004 to 0.514. Also, none of the investigated compounds were categorised as OCT2 substrates.

Toxicity. The prediction of toxicity was achieved using *pkCSM* (Tables S9–S28†) and *ProTox-II* (Tables S29–S48). AMES test is a commonly used method for the evaluation of a compound's mutagenicity, *i.e.*, carcinogenic effect.[79] Here, *pkCSM* categorised almost all pyrazolone compounds as AMES non-toxic. Also, none of the compounds were predicted as hepatotoxic and no skin sensations were observed. Furthermore, the inhibition of hERG I and II, which are encoding potassium channels, could lead to arrhythmia.[77] Here, none of the pyrazolones were identified as inhibitors of hERG I, whereas several of them were categorised as potential inhibitors of hERG II. The maximally tolerated dose for humans (log mg per kg per day) were predicted in the 0.49–0.86 range (3.1–7.2 mg per kg per day), which is according to *pkCSM* considered as high (log mg per kg per day values greater than 0.477). On the other hand, the oral rat acute toxicity (LD_{50}) values were predicted from 2.55 to 2.75 mol kg^{-1}, whereas the oral rat chronic toxicity values (the lowest dose that results in an observed adverse effect – LOAEL) were in the range from 1.28 to 3.31 (log mg per kg_bw per day). Finally, all compounds were predicted to be toxic against *T. Pyriformis*, whereas values obtained for minnow toxicity indicated none of the investigated compounds as toxic.

ProTox-II toxicity assessment was related to the prediction of oral toxicity (LD_{50} and toxicity class), organ toxicity (hepatotoxicity), toxicity endpoints (carcinogenicity, immunotoxicity, mutagenicity, and cytotoxicity), as well as Tox21-nuclear receptor signalling and stress response pathways. All compounds were categorised in toxicity class 4 with LD_{50} values of 800 mg kg^{-1}. Furthermore, all Tox21-nuclear receptor signalling and stress response pathways were observed as inactive in all cases. On the other hand, hepatotoxicity was predicted for all compounds within the class average values, whereas potential carcinogenicity was noted for half of them. Immunotoxicity and cytotoxicity predictions categorised all compounds as inactive, while mutagenicity potential was observed only in a few cases.

Bioactivity predictions

The bioactivity predictions were acquired using SwissTargetPrediction software. Generally, the SwissTargetPrediction charts revealed kinases, proteases, oxidoreductases, and G-protein coupled receptors as the main target classes. Despite the structural similarity, the results

differed from compound to compound depending on the present substituents. Bioactivity prediction charts for all compounds are provided in the ESI (Fig. S43–S47†).

Conclusions

In the present work, a series of twenty pyrazolone-type compounds **a–t** were synthesised and characterised by NMR, IR, and UV-Vis spectra. Five of them (**m, o, q, r,** and **t**) are newly synthesised compounds and they were additionally characterised by elemental microanalysis and melting points. All spectra were simulated using density functional theory and good agreement was achieved with experimental ones. Additionally, the crystal structure of compound **p** was determined by single-crystal X-ray diffraction analysis. It turned out that in the analysed pyrazolone, in one ring there is an enol- and in the other ring a keto-form. The compound forms a very strong and directional intramolecular O2–H⋯O1 hydrogen bond resulting from the tautomerisation of pyrazolone rings. The crystal packing is based on strong O–H⋯N and N–H⋯O hydrogen bonds.

In silico investigations performed on the spike, M^{pro}, and PL$_{pro}$ proteins of SARS-CoV-2 revealed higher binding affinity in comparison to selected FDA-approved drugs. Particularly, analogues **j** and **i** were identified as the most potent binders of spike protein in comparison to all investigated compounds. Among selected drugs, only lopinavir exerted a slightly higher binding affinity towards spike protein. On the other hand, derivative **d** expressed the highest *in silico* inhibitory activity against M^{pro} in comparison to all other analogues and selected drugs. Pyrazolone **l** exhibited the highest binding affinity towards PL$_{pro}$ compared to all evaluated compounds and selected drugs. These findings highlighted R^2- and R^3-substituted pyrazolone analogues as the most potent inhibitors of the SARS-CoV-2 key viral proteins, particularly those bearing –NO$_2$, –OH, and –CH$_3$ groups. Furthermore, the investigations performed on spike RBD-ACE2 complex revealed the highest binding affinity of compound **i**, whereas for ACE2 the best results were obtained for **i, o,** and **l**. These results indicate that pyrazolones could act as potential multitarget antiviral agents, blocking both reproduction and binding of SARS-CoV-2 to human cells.

The obtained *in silico* ADME/T results revealed good drug-like features, *i.e.*, water-solubility, lipophilicity, and gastrointestinal absorption. Based on the distribution and metabolism predictions, pyrazolones **a–t** were not categorised as CNS and BBB permeants, nor as inhibitors of crucial cytochrome isoenzymes, which are important features for avoiding drug side effects. Furthermore, toxicity predictions provided generally good results for almost all toxicity parameters.

The obtained results indicate the promising multitarget antiviral potential of the synthesised pyrazolone compounds against SARS-CoV-2 and represent good background for further *in vitro* experiments.

Experimental section

All chemicals were obtained either from Sigma-Aldrich Co. or Merck & Co. Pyrazolone (5-methyl-2,4-dihydro-3H-pyrazol-3-

one) was synthesised from methyl acetoacetate and hydrazine monohydrate employing a common synthetic method. The ^{1}H NMR and ^{13}C NMR spectra were recorded on a Varian Gemini spectrometer (200 MHz for ^{1}H and 50 MHz for ^{13}C) in DMSO-d_6 as solvent. The IR spectra were recorded on a PerkinElmer Spectrum One FT-IR spectrometer using the KBr plates. The UV-Vis spectra were measured within the 200–600 nm range on the Agilent Technologies, Cary 300 Series UV-Vis Spectrophotometer. Melting points of the newly synthesised compounds were determined on the Melt-Temp capillary melting points apparatus, model 1001. Elemental (C, H, N) microanalysis of new compounds was performed at the University of Belgrade, Faculty of Chemistry.

Synthetic procedure

5-Methyl-2,4-dihydro-3H-pyrazol-3-one (1 mmol) was added to the ethanolic solution of the corresponding aromatic aldehyde (0.5 mmol) with a catalytic amount of diethanolamine (20 mol%). The reaction mixture was heated to 80 °C for 3 h. After the completion of the reaction (which was monitored by thin-layer chromatography), the reaction mixture was cooled and the solid product was filtered and washed with minimal amounts of ethanol, water, and ether, respectively. In some cases, the solid products were obtained after cooling the reaction mixture. In this way, most products were obtained in the pure state. For some products, additional purification was achieved by precipitation of the products from ethanol or a mixture of ethanol and water (1 : 4). Derivative **p** crystallised from the mixture of ethanol and water (1 : 2). All products were characterised by ^{1}H NMR, ^{13}C NMR, UV-Vis, and FT-IR spectra, while derivative **p** was also characterised by X-ray crystallography. Additionally, for the new compounds, elemental microanalysis and melting points were determined. Here, spectral data for new compounds are presented, while for other derivatives are provided in the ESI.†

4-((2,3-Dihydroxyphenyl)(3-hydroxy-5-methyl-1H-pyrazol-4-yl)methyl)-5-methyl-1,2-dihydro-3H-pyrazol-3-one (m). Brown solid; m.p. = 180–182 °C; ^{1}H NMR (200 MHz, DMSO-d_6) δ: 9.14 (s, 2H), 6.98 (dd, J = 7.6, 1.7 Hz, 1H), 6.60–6.38 (m, 2H), 5.07 (s, 1H), 2.06 (s, 6H); ^{13}C NMR (50 MHz, DMSO-d_6) δ: 161.5, 144.4, 142.0, 140.4, 131.3, 120.1, 117.9, 112.7, 104.4, 27.1, 10.7; IR (KBr): ν_{max} = 3192 (stretch OH), 2928 (stretch CH), 1603 (stretch CO), 1525 (stretch CN), 1476 (bend HCC), 1436 (stretch CC), 1394 (bend HOC), 1372 (bend HNN), 1317 (stretch CO), 1285 (stretch CO), 1225 (bend HOC), 1206 (stretch CC), 1079 (bend HCC), 980 (stretch CO), 767 (torsion HNCC), 731 (torsion HOCC) cm^{-1}; simulated IR: 3355, 2932, 1672, 1508, 1465, 1419, 1352, 1330, 1275, 1257, 1218, 1210, 1070, 949, 711, 699 cm^{-1}; UV-Vis spectrum (MeOH) λ_{max} (nm) = 249, 226, 202; simulated UV-Vis spectrum: 250, 229, 206; C$_{15}$H$_{16}$N$_4$O$_4$·2H$_2$O (FW = 352.32): C, 51.13%; H, 5.72%; N, 15.90%; found: C, 50.89%; H, 5.72%; N, 15.80%.

4-((2-Hydroxy-3-methoxyphenyl)(3-hydroxy-5-methyl-1H-pyrazol-4-yl)methyl)-5-methyl-1,2-dihydro-3H-pyrazol-3-one (o). Yellow solid; m.p. = 186–188 °C; ^{1}H NMR (200 MHz, DMSO-d_6) δ: 11.22 (s, 4H), 8.47 (s, 1H), 7.12 (dd, J = 7.7, 1.5 Hz, 1H), 6.77–

6.54 (m, 2H), 5.08 (s, 1H), 3.73 (s, 3H), 2.05 (s, 6H); ^{13}C NMR (50 MHz, DMSO-d_6) δ: 161.5, 146.9, 142.8, 140.2, 131.1, 121.6, 117.8, 109.2, 104.3, 55.9, 27.1, 10.7; IR (KBr): ν_{max} = 3428 (stretch NH), 3214 (stretch OH), 2925 (stretch CH), 1592 (stretch CO), 1523 (stretch CN), 1478 (bend HCC), 1443 (bend HOC), 1361 (bend HNN), 1272 (stretch CO), 1232 (stretch CO), 1193 (bend HCC), 1166 (stretch NN), 1074 (stretch CO), 926 (stretch CO), 793 (torsion HOCC), 730 (torsion HNCC) cm^{-1}; simulated IR: 3405, 3266, 2923, 1671, 1509, 1467, 1427, 1325, 1265, 1196, 1161, 1121, 1074, 913, 739, 690 cm^{-1}; UV-Vis spectrum (MeOH) λ_{max} (nm) = 282, 249, 227, 202; simulated UV-Vis spectrum: 264, 253, 233, 205; $C_{16}H_{18}N_4O_4 \cdot 2H_2O$ (FW = 366.34): C, 52.45%; H, 6.05%; N, 15.29%; found: C, 52.84%; H, 5.96%; N, 15.54%.

4-((4-Hydroxy-3,5-dimethoxyphenyl)(3-hydroxy-5-methyl-1H-pyrazol-4-yl)methyl)-5-methyl-1,2-dihydro-3H-pyrazol-3-one (q). Orange solid; m.p. = 178–180 °C; ^{1}H NMR (200 MHz, DMSO-d_6) δ: 11.25 (s, 4H), 8.08 (s, 1H), 6.45 (d, J = 0.7 Hz, 2H), 4.72 (s, 1H), 3.62 (s, 6H), 2.05 (s, 6H); ^{13}C NMR (50 MHz, DMSO-d_6) δ: 160.9, 147.6, 139.7, 133.9, 133.8, 106.0, 104.6, 56.4, 56.2, 48.9, 33.0, 10.6; IR (KBr): ν_{max} = 3216 (stretch NH and OH), 2956 (stretch CH), 1612 (stretch CO), 1516 (bend HCC), 1457 (stretch CC), 1424 (bend HOC), 1363 (bend HNN), 1320 (stretch CO), 1213 (stretch CO), 1117 (stretch CO), 759 (torsion HOCC), 618 (torsion HNCC) cm^{-1}; simulated IR: 3399, 3334, 2918, 1684, 1504, 1423, 1365, 1324, 1311, 1205, 1114, 690, 506 cm^{-1}; UV-Vis spectrum (MeOH) λ_{max} (nm) = 248, 230, 201.5; simulated UV-Vis spectrum: 256, 233, 212; $C_{17}H_{20}N_4O_5 \cdot 2H_2O$ (FW = 396.37): C, 51.51%; H, 6.10%; N, 14.13%; found: C, 52.00%; H, 5.71%; N, 14.39%.

4-((3-Hydroxy-4,5-dimethoxyphenyl)(3-hydroxy-5-methyl-1H-pyrazol-4-yl)methyl)-5-methyl-1,2-dihydro-3H-pyrazol-3-one (r). Beige solid; m.p. = 173–175 °C; ^{1}H NMR (200 MHz, DMSO-d_6) δ: 11.30 (s, 4H), 8.89 (s, 1H), 6.26 (q, J = 2.1 Hz, 2H), 4.67 (s, 1H), 3.61 (d, J = 2.5 Hz, 6H), 2.06 (s, 6H); ^{13}C NMR (50 MHz, DMSO-d_6) δ: 161.1, 152.4, 149.8, 139.8, 139.0, 134.5, 108.9, 104.3, 103.4, 59.9, 55.7, 32.9, 10.5; IR (KBr): ν_{max} = 3400 (stretch NH), 3236 (stretch OH), 2936 (stretch CH), 1591 (stretch CO), 1541 (stretch CN), 1522 (bend HCC), 1468 (stretch CC), 1419 (bend HNN), 1338 (stretch CO), 1231 (stretch CO), 1105 (stretch CO), 999 (stretch CO), 753 (torsion HOCC) cm^{-1}; simulated IR: 3403, 3305, 2922, 1682, 1509, 1497, 1426, 1413, 1316, 1213, 1055, 997, 700 cm^{-1}; UV-Vis spectrum (MeOH) λ_{max} (nm) = 252, 231, 203; simulated UV-Vis spectrum: 253, 235, 204; $C_{17}H_{20}N_4O_5 \cdot H_2O$ (FW = 378.37): C, 53.96%; H, 5.86%; N, 14.81%; found: C, 53.43%; H, 5.95%; N, 14.6%.

4-((3,5-Dichloro-2-hydroxyphenyl)(3-hydroxy-5-methyl-1H-pyrazol-4-yl)methyl)-5-methyl-1,2-dihydro-3H-pyrazol-3-one (t). Beige solid; m.p. = 178–180 °C; ^{1}H NMR (200 MHz, DMSO-d_6) δ: 11.01 (s, 5H), 7.37 (d, J = 2.6 Hz, 1H), 7.25 (d, J = 2.6 Hz, 1H), 5.02 (s, 1H), 2.04 (s, 6H); ^{13}C NMR (50 MHz, DMSO-d_6) δ: 160.8, 150.1, 139.9, 135.8, 128.1, 126.0, 122.0, 121.8, 102.9, 29.4, 10.8; IR (KBr): ν_{max} = 3368 (stretch NH and OH), 1601 (stretch CO), 1577 (stretch CC), 1541 (stretch CN), 1517 (bend HCC), 1464 (stretch CC), 1410 (bend HCH), 1387 (bend HNN), 1355 (bend HNN), 1312 (stretch CO), 1257 (stretch CO), 1228 (bend HOC), 1161 (stretch CCl), 1143 (stretch NN), 1095 (stretch CC), 769 (torsion HOCC), 734 (torsion HNCC) cm^{-1}; simulated IR: 3411,

3266, 1672, 1617, 1509, 1445, 1403, 1391, 1354, 1324, 1245, 1220, 1180, 1138, 1123, 1083, 706, 690 cm^{-1}; UV-Vis spectrum (MeOH) λ_{max} (nm) = 253, 232, 202; simulated UV-Vis spectrum: 267, 239, 209; $C_{15}H_{14}Cl_2N_4O_3 \cdot 4H_2O$ (FW = 441.20): C, 40.83%; H, 5.03%; N, 12.70%; found: C, 40.75%; H, 5.27%; N, 12.59%.

Single-crystal X-ray diffraction

Single-crystal X-ray diffraction data for compound **p** were collected on a Bruker APEX-II CCD diffractometer with mono-chromatised MoKα radiation (λ = 0.71073 Å). Data reduction and empirical absorption correction were performed with the CrysAlisPRO program package.[80] The structure was solved by direct methods using SHELXS and refined on F^2 by full-matrix least-squares using SHELXL.[81] The compound was refined as a two-component inversion twin. H atoms bonded to C atoms were placed in geometrically calculated positions and refined using the riding model with U_{iso} values constrained to 1.2U_{eq} or 1.5U_{eq} of the parent C atoms. The H atoms bonded to O and N atoms were freely refined. Structural analysis was carried out in PLATON[82] and Mercury[83] which was also used for molecular graphics. Crystallographic details are summarised in Table S2.† X-ray diffraction data of the compound **p** have been deposited at the Cambridge Crystallographic Data Centre and assigned CCDC 2132092† deposition number.

DFT calculations

The Gaussian 09 program package was used to perform all necessary calculations.[84] The equilibrium geometries of all pyrazolone analogues were calculated using B3LYP functional in the conjunction with the 6-311+g(d,p) basis set.[85–87] To confirm the local minima of the investigated compounds, vibrational analysis was performed (no imaginary frequencies were found). The optimised geometries in the gas phase were used for the simulation of IR spectra (Fig. S21–S23†). IR bands were scaled using the scaling factor obtained using the least-squares method and amount of 0.97. The SMD solvation model implemented in the Gaussian 09 package was utilised to perform calculations in methanol, as well as for the TD-DFT simulation of UV-Vis spectra since it was experimentally used as a solvent.[88]

Molecular docking

The crystal structures of all proteins were acquired from the RSC protein data bank: SARS-CoV-2 spike glycoprotein with an RBD (S) (PDB ID: 6VSB),[89] the M^{pro} in complex with an inhibitor N3 (PDB-ID: 6LU7),[10] PL$_{pro}$ (PDB-ID: 6WZU),[90] inhibitor bound ACE2 (PDB-ID: 1R4L),[91] spike RBD-ACE2 complex (PDB-ID: 6LZG).[92] For the preparation of the proteins, as well as for analysis of ligand–macromolecule interactions UCSF Chimera v1.16 software was used, while Discovery Studio Visualizer was used for 2D interpretations.[93–95]

CastP server (**https://sts.bioe.uic.edu/castp/**)[67] and CHARMM-GUI (**https://www.charmm-gui.org**)[68] were used for the prediction of active site pockets and respective amino acid residues. All compounds were subjected to conformational analysis using VeraChem's Vconf 2.0 (VeraChem LLC, Germantown, MA, USA) where the conformations within the

threshold of 5 kcal mol^{-1} were selected for molecular docking. Selected conformations of each compound were subjected to blind docking with the target proteins using AutoDock Vina.[96] The grids for the target proteins were set to ensure the whole macromolecules are placed in the corresponding grid box, with a spacing of 1.000 Å. Additionally, selected FDA-approved drugs lopinavir, remdesivir, chloroquine, and favipiravir (Pub-Chem CIDs: 92727, 121304016, 2719, and 492405, respectively) were subjected to docking using the same methodology as described for pyrazolones. The selection was made based on their application in the COVID-19 treatment.[97]

In silico ADME/T profiling and bioactivity prediction

The insight into physicochemical, pharmacological, toxicological, and drug-like features of pyrazolone derivatives was achieved using *SwissADME* (**https://www.SwissADME.ch/**) and *pkCSM* (**https://biosig.unimelb.edu.au/pkCSM/prediction**) web tools.[77,98] These services were chosen since they provide relevant pharmacokinetic data for small molecule drug candidates (*i.e.*, absorption, distribution, metabolism, excretion, and toxicity).

Also, the *ProTox-II* web service (**https://toxnew.charite.de/protox_II/index.php?site=compound_input**) was employed for additional evaluation of compounds toxicity.[99] The prediction of bioactivity was performed using SwissTargetPrediction. The structures of pyrazolone compounds **a–t** were converted to simplified molecular-input line entry specification (SMILES) nomenclature and as such imported into selected web services.

Author contributions

Conceptualization, V. P.; methodology, V. P., D. S., and. Z. P.; validation, J. B., and V. M.; formal analysis, V. P, G. B., S. N., and J.B.; investigation, J. B., V. M., D. S., G. B., S. N., and S. T.; resources, V. P., and Z. P.; data curation, J. B. and V. P.; writing—original draft preparation J. B., V. P., and S. N.; writing—review and editing, V. P., Z. P., D. S., and G. B.; visualization, V. P., J. B., and G. B.; supervision, V. P.; project administration, V. P. and Z. P.; funding acquisition, V. P. and Z. P. All authors have read and agreed to the published version of the manuscript.

Conflicts of interest

There are no conflicts to declare.

Acknowledgements

References

1 A. Sheikh, J. McMenamin, B. Taylor and C. Robertson, *Lancet*, 2021, **397**, 2461–2462.

2 N. Ferguson, A. Ghani, A. Cori, A. Hogan, W. Hinsley and E. Volz, *Imp. Coll. COVID-19 Response Team*, 2021, pp. 1–10.

3 J. R. C. Pulliam, C. van Schalkwyk, N. Govender, A. von Gottberg, C. Cohen, M. J. Groome, J. Dushoff, K. Mlisana and H. Moultrie, *Science*, 2022, **376**(6593), eabn4947.

4 B. Meng, A. Abdullahi, I. A. T. M. Ferreira, N. Goonawardane, A. Saito, I. Kimura, D. Yamasoba, P. P. Gerber, S. Fatihi, S. Rathore, S. K. Zepeda, G. Papa, S. A. Kemp, T. Ikeda, M. Toyoda, T. S. Tan, J. Kuramochi, S. Mitsunaga, T. Ueno, K. Shirakawa, A. Takaori-Kondo, T. Brevini, D. L. Mallery, O. J. Charles, S. Baker, G. Dougan, C. Hess, N. Kingston, P. J. Lehner, P. A. Lyons, N. J. Matheson, W. H. Ouwehand, C. Saunders, C. Summers, J. E. D. Thaventhiran, M. Toshner, M. P. Weekes, P. Maxwell, A. Shaw, A. Bucke, J. Calder, L. Canna, J. Domingo, A. Elmer, S. Fuller, J. Harris, S. Hewitt, J. Kennet, S. Jose, J. Kourampa, A. Meadows, C. O'Brien, J. Price, C. Publico, R. Rastall, C. Ribeiro, J. Rowlands, V. Ruffolo, H. Tordesillas, B. Bullman, B. J. Dunmore, S. Gräf, J. Hodgson, C. Huang, K. Hunter, E. Jones, E. Legchenko, C. Matara, J. Martin, F. Mescia, C. O'Donnell, L. Pointon, J. Shih, R. Sutcliffe, T. Tilly, C. Treacy, Z. Tong, J. Wood, M. Wylot, A. Betancourt, G. Bower, C. Cossetti, A. De Sa, M. Epping, S. Fawke, N. Gleadall, R. Grenfell, A. Hinch, S. Jackson, I. Jarvis, B. Krishna, F. Nice, O. Omarjee, M. Perera, M. Potts, N. Richoz, V. Romashova, L. Stefanucci, M. Strezlecki, L. Turner, E. M. D. D. De Bie, K. Bunclark, M. Josipovic, M. Mackay, H. Butcher, D. Caputo, M. Chandler, P. Chinnery, D. Clapham-Riley, E. Dewhurst, C. Fernandez, A. Furlong, B. Graves, J. Gray, S. Hein, T. Ivers, E. Le Gresley, R. Linger, M. Kasanicki, R. King, N. Kingston, S. Meloy, A. Moulton, F. Muldoon, N. Ovington, S. Papadia, C. J. Penkett, I. Phelan, V. Ranganath, R. Paraschiv, A. Sage, J. Sambrook, I. Scholtes, K. Schon, H. Stark, K. E. Stirrups, P. Townsend, N. Walker, J. Webster, E. P. Butlertanaka, Y. L. Tanaka, J. Ito, K. Uriu, Y. Kosugi, M. Suganami, A. Oide, M. Yokoyama, M. Chiba, C. Motozono, H. Nasser, R. Shimizu, K. Kitazato, H. Hasebe, T. Irie, S. Nakagawa, J. Wu, M. Takahashi, T. Fukuhara, K. Shimizu, K. Tsushima, H. Kubo, Y. Kazuma, R. Nomura, Y. Horisawa, K. Nagata, Y. Kawai, Y. Yanagida, Y. Tashiro, K. Tokunaga, S. Ozono, R. Kawabata, N. Morizako, K. Sadamasu, H. Asakura, M. Nagashima, K. Yoshimura, P. Cárdenas, E. Muñoz, V. Barragan, S. Márquez, B. Prado-Vivar, M. Becerra-Wong, M. Caravajal, G. Trueba, P. Rojas-Silva, M. Grunauer, B. Gutierrez, J. J. Guadalupe, J. C. Fernández-Cadena, D. Andrade-Molina, M. Baldeon, A. Pinos, J. E. Bowen, A. Joshi, A. C. Walls, L. Jackson, D. Martin, K. G. C. Smith, J. Bradley, J. A. G. Briggs, J. Choi, E. Madissoon, K. B. Meyer, P. Mlcochova, L. Ceron-Gutierrez, R. Doffinger, S. A. Teichmann, A. J. Fisher, M. S. Pizzuto, A. de Marco, D. Corti, M. Hosmillo, J. H. Lee, L. C. James, L. Thukral, D. Veesler, A. Sigal, F. Sampaziotis, I. G. Goodfellow, N. J. Matheson, K. Sato and R. K. Gupta, *Nature*, 2022, **603**, 706–714.

5 Y. Cao, J. Wang, F. Jian, T. Xiao, W. Song, A. Yisimayi, W. Huang, Q. Li, P. Wang, R. An, J. Wang, Y. Wang, X. Niu, S. Yang, H. Liang, H. Sun, T. Li, Y. Yu, Q. Cui, S. Liu, X. Yang, S. Du, Z. Zhang, X. Hao, F. Shao, R. Jin, X. Wang, J. Xiao, Y. Wang and X. S. Xie, *Nature*, 2022, **602**, 657–663.

6 L. Liu, S. Iketani, Y. Guo, J. F. W. Chan, M. Wang, L. Liu, Y. Luo, H. Chu, Y. Huang, M. S. Nair, J. Yu, K. K. H. Chik, T. T.-T. Yuen, C. Yoon, K. K. W. To, H. Chen, M. T. Yin, M. E. Sobieszczyk, Y. Huang, H. H. Wang, Z. Sheng, K.-Y. Yuen and D. D. Ho, *Nature*, 2022, **602**, 676–681.

7 S. Cele, L. Jackson, D. S. Khoury, K. Khan, T. Moyo-Gwete, H. Tegally, J. E. San, D. Cromer, C. Scheepers, D. G. Amoako, F. Karim, M. Bernstein, G. Lustig, D. Archary, M. Smith, Y. Ganga, Z. Jule, K. Reedoy, S.-H. Hwa, J. Giandhari, J. M. Blackburn, B. I. Gosnell, S. S. Abdool Karim, W. Hanekom, M.-A. Davies, M. Hsiao, D. Martin, K. Mlisana, C. K. Wibmer, C. Williamson, D. York, R. Harrichandparsad, K. Herbst, P. Jeena, T. Khoza, H. Kløverpris, A. Leslie, R. Madansein, N. Magula, N. Manickchund, M. Marakalala, M. Mazibuko, M. Moshabela, N. Mthabela, K. Naidoo, Z. Ndhlovu, T. Ndung'u, N. Ngcobo, K. Nyamande, V. Patel, T. Smit, A. Steyn, E. Wong, A. von Gottberg, J. N. Bhiman, R. J. Lessells, M.-Y. S. Moosa, M. P. Davenport, T. de Oliveira, P. L. Moore and A. Sigal, *Nature*, 2022, **602**, 654–656.

8 U. Rutwick Surya and N. Praveen, *VirusDisease*, 2021, **32**, 46–54.

9 M. Hosseini, W. Chen, D. Xiao and C. Wang, *Precision Clinical Medicine*, 2021, **4**, 1–16.

10 Z. Jin, X. Du, Y. Xu, Y. Deng, M. Liu, Y. Zhao, B. Zhang, X. Li, L. Zhang, C. Peng, Y. Duan, J. Yu, L. Wang, K. Yang, F. Liu, R. Jiang, X. Yang, T. You, X. Liu, X. Yang, F. Bai, H. Liu, X. Liu, L. W. Guddat, W. Xu, G. Xiao, C. Qin, Z. Shi, H. Jiang, Z. Rao and H. Yang, *Nature*, 2020, **582**, 289–293.

11 J. Qiao, Y.-S. Li, R. Zeng, F.-L. Liu, H.-R. Luo, C. Huang, Y.-F. Wang, J. Zhang, B. Quan, C. Shen, X. Mao, X. Liu, W. Sun, W. Yang, X. Ni, K. Wang, L. Xu, Z.-L. Duan, Q.-C. Zou and S. Yang, *Science*, 2021, **371**, eabf1611.

12 M. E. Sobhia, K. Ghosh, S. Sivangula, S. Kumar and H. Singh, *J. Biomol. Struct. Dyn.*, 2021, 1–11.

13 D. W. Kneller, G. Phillips, H. M. O'Neill, R. Jedrzejczak, L. Stols, P. Langan, A. Joachimiak, L. Coates and A. Kovalevsky, *Nat. Commun.*, 2020, **11**, 7–12.

14 L. Zhang, D. Lin, Y. Kusov, Y. Nian, Q. Ma, J. Wang, A. Von Brunn, P. Leyssen, K. Lanko, J. Neyts, A. De Wilde, E. J. Snijder, H. Liu and R. Hilgenfeld, *J. Med. Chem.*, 2020, **63**, 4562–4578.

15 M. D. Sacco, C. Ma, P. Lagarias, A. Gao, J. A. Townsend, X. Meng, P. Dube, X. Zhang, Y. Hu, N. Kitamura, B. Hurst, B. Tarbet, M. T. Marty, A. Kolocouris, Y. Xiang, Y. Chen and J. Wang, *Sci. Adv.*, 2020, **6**, eabe0751.

16 Z. Fu, B. Huang, J. Tang, S. Liu, M. Liu, Y. Ye, Z. Liu, Y. Xiong, W. Zhu, D. Cao, J. Li, X. Niu, H. Zhou, Y. J. Zhao, G. Zhang and H. Huang, *Nat. Commun.*, 2021, **12**, 488.

17 D. Shin, R. Mukherjee, D. Grewe, D. Bojkova, K. Baek, A. Bhattacharya, L. Schulz, M. Widera, A. R. Mehdipour, G. Tascher, P. P. Geurink, A. Wilhelm, G. J. van der Heden

van Noort, H. Ovaa, S. Müller, K. P. Knobeloch, K. Rajalingam, B. A. Schulman, J. Cinatl, G. Hummer, S. Ciesek and I. Dikic, *Nature*, 2020, **587**, 657–662.

18 K. Al Adem, A. Shanti, C. Stefanini and S. Lee, *Pharmaceuticals*, 2020, **13**, 1–34.

19 M. Gheblawi, K. Wang, A. Viveiros, Q. Nguyen, J.-C. Zhong, A. J. Turner, M. K. Raizada, M. B. Grant and G. Y. Oudit, *Circ. Res.*, 2020, **126**, 1456–1474.

20 J. Yang, S. J. L. Petitjean, M. Koehler, Q. Zhang, A. C. Dumitru, W. Chen, S. Derclaye, S. P. Vincent, P. Soumillion and D. Alsteens, *Nat. Commun.*, 2020, **11**, 4541.

21 S. Choudhary, Y. S. Malik and S. Tomar, *Front. Immunol.*, 2020, **11**, 1664.

22 S. Bharadwaj, E. I. Azhar, M. A. Kamal, L. H. Bajrai, A. Dubey, K. Jha, U. Yadava, S. G. Kang and V. D. Dwivedi, *J. Biomol. Struct. Dyn.*, 2020, 1–16.

23 Y. Han and P. Král, *ACS Nano*, 2020, **14**, 5143–5147.

24 G. Jaiswal and V. Kumar, *PLoS One*, 2020, **15**, 1–15.

25 F. X. Domínguez-Villa, N. A. Durán-Iturbide and J. G. Ávila-Zárraga, *Bioorg. Chem.*, 2021, **106**, 104497.

26 R. Nandini Asha, B. Ravindran Durai Nayagam and N. Bhuvanesh, *Bioorg. Chem.*, 2021, **112**, 104967.

27 A. Ali, N. Sepay, M. Afzal, N. Sepay, A. Alarifi, M. Shahid and M. Ahmad, *Bioorg. Chem.*, 2021, **110**, 104772.

28 N. Atatreh, S. Hasan, B. R. Ali and M. A. Ghattas, *Acta Pharm.*, 2021, **71**, 325–333.

29 V. A. Obakachi, N. D. Kushwaha, B. Kushwaha, M. C. Mahlalela, S. R. Shinde, I. Kehinde and R. Karpoormath, *J. Mol. Struct.*, 2021, **1241**, 130665.

30 R. Ramajayam, K. P. Tan, H. G. Liu and P. H. Liang, *Bioorg. Med. Chem.*, 2010, **18**, 7849–7854.

31 V. Kumar, K. P. Tan, Y. M. Wang, S. W. Lin and P. H. Liang, *Bioorg. Med. Chem.*, 2016, **24**, 3035–3042.

32 J. Sahoo, C. R. Sahoo, P. K. Nandini Sarangi, S. K. Prusty, R. N. Padhy and S. K. Paidesetty, *Eur. J. Med. Chem.*, 2020, **186**, 111911.

33 X. Fan, X. Zhang, L. Zhou, K. A. Keith, E. R. Kern and P. F. Torrence, *Bioorg. Med. Chem. Lett.*, 2006, **16**, 3224–3228.

34 H. E. Gaffer, S. Abdel-Fattah, H. A. Etman and E. Abdel-Latif, *J. Heterocycl. Chem.*, 2017, **54**, 331–340.

35 H. M. Aly, N. M. Saleh and H. A. Elhady, *Eur. J. Med. Chem.*, 2011, **46**, 4566–4572.

36 N. A. Khalil, E. M. Ahmed, K. O. Mohamed, Y. M. Nissan and S. A. B. Zaitone, *Bioorg. Med. Chem.*, 2014, **22**, 2080–2089.

37 M. T. El Sayed, M. A. M. S. El-Sharief, E. S. Zarie, N. M. Morsy, A. R. Elsheakh, A. Voronkov, V. Berishvili and G. S. Hassan, *Bioorg. Med. Chem. Lett.*, 2018, **28**, 952–957.

38 M. H. Norman, L. Liu, M. Lee, N. Xi, I. Fellows, N. D. D'Angelo, C. Dominguez, K. Rex, S. F. Bellon, T. S. Kim and I. Dussault, *J. Med. Chem.*, 2012, **55**, 1858–1867.

39 M. A. Abdelgawad, M. B. Labib, W. A. M. Ali, G. Kamel, A. A. Azouz and E. S. EL-Nahass, *Bioorg. Chem.*, 2018, **78**, 103–114.

40 K. Ochiai, S. Takita, A. Kojima, T. Eiraku, N. Ando, K. Iwase, T. Kishi, A. Ohinata, Y. Yageta, T. Yasue, D. R. Adams and Y. Kohno, *Bioorg. Med. Chem. Lett.*, 2012, **22**, 5833–5838.

41 X. K. Qian, J. Zhang, P. F. Song, Y. S. Zhao, H. Y. Ma, Q. Jin, D. D. Wang, X. Q. Guan, S. Y. Li, X. Z. Bao and L. W. Zou, *Bioorg. Med. Chem.*, 2021, **40**, 116187.

42 T. M. A. Eldebss, A. M. Farag, M. M. Abdalla and A. A. Khedr, *J. Heterocycl. Chem.*, 2019, **56**, 765–780.

43 Z. T. Muhseen, S. Kadhim, Y. I. Yahiya, E. A. Alatawi, F. F. Aba Alkhayl and A. Almatroudi, *Biology*, 2021, **10**, 1310.

44 H. You, X. Su and G. Su, *Arch. Pharm.*, 2020, **353**, 1–10.

45 Z. Zhou and Y. Zhang, *J. Chil. Chem. Soc.*, 2015, **60**, 2992–2996.

46 A. Vafaee, A. Davoodnia and M. Pordel, *Res. Chem. Intermed.*, 2015, **41**, 8343–8354.

47 J. Safaei-Ghomi, B. Khojastehbakht-Koopaei and S. Zahedi, *Chem. Heterocycl. Compd.*, 2015, **51**, 34–38.

48 R. Ramesh, N. Nagasundaram, D. Meignanasundar, P. Vadivel and A. Lalitha, *Res. Chem. Intermed.*, 2017, **43**, 1767–1782.

49 M. Zarghani and B. Akhlaghinia, *RSC Adv.*, 2015, **5**, 87769–87780.

50 J. Safaei-Ghomi, B. Khojastehbakht-Koopaei and H. Shahbazi-Alavi, *RSC Adv.*, 2014, **4**, 46106–46113.

51 R. Khalifeh, R. Shahimoridi and M. Rajabzadeh, *Catal. Lett.*, 2019, **149**, 2864–2872.

52 Z. Zhou and Y. Zhang, *Green Chem. Lett. Rev.*, 2014, **7**, 18–23.

53 Z.-Z. Sheng, M.-M. Huang, T. Xue, F. Xia and H.-H. Wu, *RSC Adv.*, 2020, **10**, 34910–34915.

54 J. E. Gannon, M. C. Adams and E. O. Bennett, *Microbios*, 1978, **23**, 7–18.

55 R. J. West and S. J. Gonsior, *Environ. Toxicol. Chem.*, 1996, **15**, 472–480.

56 F. Mancia, P. Vasileios, O. B. Clarke and J. P. Vendome, Rational drug design targeting resistant Gram-negative bacterial infections to polymyxin-class antibiotics, *WIPO Pat.*, WO2017083859A1, 2017.

57 A. M. Zonouz, M. Beiranvand, R. Mohammad-Rezaei and S. Naderi, *Lett. Org. Chem.*, 2020, **17**, 548–554.

58 W. Wang, S.-X. Wang, X.-Y. Qin and J.-T. Li, *Synth. Commun.*, 2005, **35**, 1263–1269.

59 R. Ramesh, N. Nagasundaram, D. Meignanasundar, P. Vadivel and A. Lalitha, *Res. Chem. Intermed.*, 2017, **43**, 1767–1782.

60 E. Soleimani, S. Ghorbani, M. Taran and A. Sarvary, *C. R. Chim.*, 2012, **15**, 955–961.

61 H.-K. Fun, R. Kia, K. S. Girish and B. Kalluraya, *Acta Crystallogr., Sect. E: Struct. Rep. Online*, 2009, **65**, o66–o67.

62 B. Kumar, H. Mahajan, S. Paul, R. Kant and V. K. Gupta, *Acta Crystallogr., Sect. E: Crystallogr. Commun.*, 2015, **71**, o805–o806.

63 H.-K. Fun, S. R. Jebas, K. S. Girish and B. Kalluraya, *Acta Crystallogr., Sect. E: Struct. Rep. Online*, 2008, **64**, o2301–o2302.

64 C. Pettinari, F. Marchetti, R. Pettinari, D. Martini, A. Drozdov and S. Troyanov, *J. Chem. Soc., Dalton Trans.*, 2001, 1790–1797.

65 J. Bernstein, R. E. Davis, L. Shimoni and N.-L. Chang, *Angew. Chem., Int. Ed. Engl.*, 1995, **34**, 1555–1573.

66 G. A. Bogdanović, B. D. Ostojić and S. B. Novaković, *Cryst. Growth Des.*, 2018, **18**, 1303–1314.

67 W. Tian, C. Chen, X. Lei, J. Zhao and J. Liang, *Nucleic Acids Res.*, 2018, **46**, W363–W367.

68 S. Jo, T. Kim, V. G. Iyer and W. Im, *J. Comput. Chem.*, 2008, **29**, 1859–1865.

69 P. K. Panda, M. N. Arul, P. Patel, S. K. Verma, W. Luo, H.-G. Rubahn, Y. K. Mishra, M. Suar and R. Ahuja, *Sci. Adv.*, 2020, **6**, 1–15.

70 H. Yang, W. Xie, X. Xue, K. Yang, J. Ma, W. Liang, Q. Zhao, Z. Zhou, D. Pei, J. Ziebuhr, R. Hilgenfeld, K. Y. Yuen, L. Wong, G. Gao, S. Chen, Z. Chen, D. Ma, M. Bartlam and Z. Rao, *PLoS Biol.*, 2005, **3**, e324.

71 J. Lan, J. Ge, J. Yu, S. Shan, H. Zhou, S. Fan, Q. Zhang, X. Shi, Q. Wang, L. Zhang and X. Wang, *Nature*, 2020, **581**, 215–220.

72 C. A. Lipinski, F. Lombardo, B. W. Dominy and P. J. Feeney, *Adv. Drug Delivery Rev.*, 1997, **23**, 3–25.

73 A. K. Ghose, V. N. Viswanadhan and J. J. Wendoloski, *J. Comb. Chem.*, 1999, **1**, 55–68.

74 D. F. Veber, S. R. Johnson, H.-Y. Cheng, B. R. Smith, K. W. Ward and K. D. Kopple, *J. Med. Chem.*, 2002, **45**, 2615–2623.

75 A. Finch and P. Pillans, *Aust. Prescr.*, 2014, **37**, 137–139.

76 A. Mansoor and N. Mahabadi, *Volume of Distribution*, Treasure Island, FL, 2022.

77 D. E. V. Pires, T. L. Blundell and D. B. Ascher, *J. Med. Chem.*, 2015, **58**, 4066–4072.

78 P. Manikandan and S. Nagini, *Curr. Drug Targets*, 2018, **19**, 38–54.

79 K. Mortelmans and E. Zeiger, *Mutat. Res., Fundam. Mol. Mech. Mutagen.*, 2000, **455**, 29–60.

80 Rigaku Oxford Diffraction, *CrysAlisPro Softw. Syst*, Rigaku Corp., Oxford, UK, 2015.

81 G. M. Sheldrick, *Acta Crystallogr., Sect. C: Struct. Chem.*, 2015, **71**, 3–8.

82 A. L. Spek, *Acta Crystallogr., Sect. C: Struct. Chem.*, 2009, **65**, 148–155.

83 C. F. MacRae, I. Sovago, S. J. Cottrell, P. T. A. Galek, P. McCabe, E. Pidcock, M. Platings, G. P. Shields, J. S. Stevens, M. Towler and P. A. Wood, *J. Appl. Crystallogr.*, 2020, **53**, 226–235.

84 M. J. Frisch, G. W. Trucks, H. B. Schlegel, G. E. Scuseria, M. a. Robb, J. R. Cheeseman, G. Scalmani, V. Barone, G. a. Petersson, H. Nakatsuji, X. Li, M. Caricato, a. V. Marenich, J. Bloino, B. G. Janesko, R. Gomperts, B. Mennucci, H. P. Hratchian, J. V. Ortiz, a. F. Izmaylov, J. L. Sonnenberg, D. Williams-Young, F. Ding, F. Lipparini, F. Egidi, J. Goings, B. Peng, A. Petrone, T. Henderson, D. Ranasinghe, V. G. Zakrzewski, J. Gao, N. Rega, G. Zheng, W. Liang, M. Hada, M. Ehara, K. Toyota, R. Fukuda, J. Hasegawa, M. Ishida, T. Nakajima, Y. Honda, O. Kitao, H. Nakai, T. Vreven, K. Throssell, J. a. Montgomery Jr, J. E. Peralta, F. Ogliaro, M. J. Bearpark, J. J. Heyd, E. N. Brothers, K. N. Kudin, V. N. Staroverov, T. a. Keith, R. Kobayashi, J. Normand, K. Raghavachari, a. P. Rendell, J. C. Burant, S. S. Iyengar, J. Tomasi, M. Cossi, J. M. Millam, M. Klene, C. Adamo,

R. Cammi, J. W. Ochterski, R. L. Martin, K. Morokuma, O. Farkas, J. B. Foresman and D. J. Fox, *Gaussian 16, Revision C.01*, Gaussian, Inc., Wallingford, 2016.

85 A. D. Becke, *J. Chem. Phys.*, 1993, **98**, 5648–5652.

86 C. Lee, W. Yang and R. G. Parr, *Phys. Rev. B: Condens. Matter Mater. Phys.*, 1988, **37**, 785–789.

87 T. H. Dunning, *J. Chem. Phys.*, 1989, **90**, 1007–1023.

88 A. V. Marenich, C. J. Cramer and D. G. Truhlar, *J. Phys. Chem. B*, 2009, **113**, 4538–4543.

89 D. Wrapp, N. Wang, K. S. Corbett, J. A. Goldsmith, C.-L. Hsieh, O. Abiona, B. S. Graham and J. S. McLellan, *Science*, 2020, **367**, 1260–1263.

90 J. Osipiuk, S.-A. Azizi, S. Dvorkin, M. Endres, R. Jedrzejczak, K. A. Jones, S. Kang, R. S. Kathayat, Y. Kim, V. G. Lisnyak, S. L. Maki, V. Nicolaescu, C. A. Taylor, C. Tesar, Y.-A. Zhang, Z. Zhou, G. Randall, K. Michalska, S. A. Snyder, B. C. Dickinson and A. Joachimiak, *Nat. Commun.*, 2021, **12**, 743.

91 P. Towler, B. Staker, S. G. Prasad, S. Menon, J. Tang, T. Parsons, D. Ryan, M. Fisher, D. Williams, N. A. Dales, M. A. Patane and M. W. Pantoliano, *J. Biol. Chem.*, 2004, **279**, 17996–18007.

92 Q. Wang, Y. Zhang, L. Wu, S. Niu, C. Song, Z. Zhang, G. Lu, C. Qiao, Y. Hu, K.-Y. Yuen, Q. Wang, H. Zhou, J. Yan and J. Qi, *Cell*, 2020, **181**, 894–904.e9.

93 D. Simijonović, E. E. Vlachou, Z. D. Petrović, D. J. Hadjipavlou-Litina, K. E. Litinas, N. Stanković, N. Mihović and M. P. Mladenović, *Bioorg. Chem.*, 2018, **80**, 741–752.

94 E. F. Pettersen, T. D. Goddard, C. C. Huang, G. S. Couch, D. M. Greenblatt, E. C. Meng and T. E. Ferrin, *J. Comput. Chem.*, 2004, **25**, 1605–1612.

95 S. D. D. S. BIOVIA, *Dassault Systèmes, Discovery Studio Visualizer, v 21.1.0.20298*.

96 O. Trott and A. J. Olson, *J. Comput. Chem.*, 2010, **31**, 455–461.

97 Faheem, B. K. Kumar, K. V. G. C. Sekhar, S. Kunjiappan, J. Jamalis, R. Balaña-Fouce, B. L. Tekwani and M. Sankaranarayanan, *Bioorg. Chem.*, 2020, **104**, 104269.

98 A. Daina, O. Michielin and V. Zoete, *Sci. Rep.*, 2017, **7**, 1–13.

99 P. Banerjee, A. O. Eckert, A. K. Schrey and R. Preissner, *Nucleic Acids Res.*, 2018, **46**, W257–W263.

© 2022 The Author(s). Published by the Royal Society of Chemistry